JOURNAL OF GEOPHYSICAL RESEARCH, VOL. 114, E00B32, doi:10.1029/2008JE003073, 2009

Gravity waves in the upper atmosphere of Venus revealed by CO_2 nonlocal thermodynamic equilibrium emissions

R. F. Garcia,[1] P. Drossart,[2] G. Piccioni,[3] M. López-Valverde,[4] and G. Occhipinti[5]

Received 10 January 2008; revised 29 December 2008; accepted 14 January 2009; published 17 March 2009.

[1] The imaging capabilities of the Visible and Infrared Thermal Imaging Spectrometer-Mapper (VIRTIS-M) onboard Venus Express mission are used to analyze perturbations of CO_2 nonlocal thermodynamic equilibrium emissions in the thermosphere of Venus. These emissions with a wavelength of 4.3 μm originate from the 110–140 km altitude range and are sensitive to density perturbations. They show wave-like perturbations of about 0.5% root-mean-square amplitude of the background signal with horizontal wavelengths in the 90–400 km range. The horizontal phase velocities are similar in magnitude and direction from one orbit to the next, with averages of 70 m/s westward and 30 m/s northward. The geographical wave distribution and the orientation of wavefronts demonstrate that the polar vortex at work in the cloud layer is the source of these gravity waves. The large westward zonal phase velocity in the 0900–1500 local time range argues in favor of the superrotation dynamics within 30° from the south pole to an altitude of at least 115 km. The gravity wave dispersion relation and the geographical distribution of wavefront amplitudes suggest the presence of a solar to antisolar wind close to the south pole. Because the centroid altitude and the sensitivity of these emissions to gravity wave perturbations are only roughly estimated, it is not possible to make a quantitative estimate of the upward energy transfer. However, this study demonstrates the strong influence of the polar vortex on the circulation in the atmosphere of Venus up to the thermosphere.

Citation: Garcia, R. F., P. Drossart, G. Piccioni, M. López-Valverde, and G. Occhipinti (2009), Gravity waves in the upper atmosphere of Venus revealed by CO_2 nonlocal thermodynamic equilibrium emissions, *J. Geophys. Res.*, *114*, E00B32, doi:10.1029/2008JE003073.

1. Introduction

[2] The atmosphere of Venus is a very active and turbulent medium which is expected to show competition between subsolar to antisolar and superrotation circulations [*Gierasch et al.*, 1997]. The clues to understanding the mechanisms of this competition are in the lower thermosphere of Venus. However, up to now, the dynamics of Venus' lower thermosphere have only been investigated by indirect evidence relying mainly on the distribution of neutral species, temperature and O_2 airglow [*Bougher and Borucki*, 1994; *Bougher et al.*, 1997]. The nonlocal thermodynamic equilibrium (non-LTE) emissions of CO_2 on the dayside upper atmosphere of Venus provide a way of investigating the structure and dynamics of Venus' lower thermosphere [*Roldán et al.*, 2000; *Gilli et al.*, 2009]. Moreover, the imaging capabilities of the Visible and Infrared Thermal Imaging Spectrometer-Mapper (VIRTIS-M) onboard the Venus Express mission can be used to investigate the evolution over time of these emissions on successive images taken at nadir or at the limb [*Drossart et al.*, 2004, 2007].

[3] The models of thermosphere circulation [*Zhang et al.*, 1996; *Bougher et al.*, 1997] are sensitive to the dynamics and breaking of atmospheric gravity waves. These waves have been observed in Venus troposphere [*Gierasch*, 1987; *Young et al.*, 1987; *Hinson and Jenkins*, 1995] and thermosphere [*Kasprzak et al.*, 1993] by different exploration missions. The modeling of the upper atmosphere gravity wave propagation suggests a source in the lower atmosphere [*Mayr et al.*, 1988] which is probably related to the turbulence in the cloud layer [*Woo et al.*, 1980, 1982]. Gravity waves are also used to explain the atmospheric superrotation [*Alexander*, 1992].

[4] The CO_2 non-LTE emissions, which are mainly sensitive to density perturbations [*Roldán et al.*, 2000], provide a unique opportunity for direct observation of the dynamics of gravity waves in the 110–140 km altitude range. Despite the limitations induced by the integrated information content along the line of sight, and the restricted knowledge on both the space/time distribution of these emissions [*Drossart et al.*,

[1]Laboratoire de Dynamique Terrestre et Planétaire, UMR5562, Observatoire Midi-Pyrénées, Université de Toulouse, CNRS, Toulouse, France.
[2]LESIA, Observatoire de Paris, UPMC, Université Paris-Diderot, CNRS, Meudon, France.
[3]INAF, IASF, Rome, Italy.
[4]Instituto de Astrofísica de Andalucía, CISC, Granada, Spain.
[5]Institut de Physique du Globe de Paris, Université Denis Diderot Paris 7, Paris, France.

0148-0227/09/2008JE003073$09.00

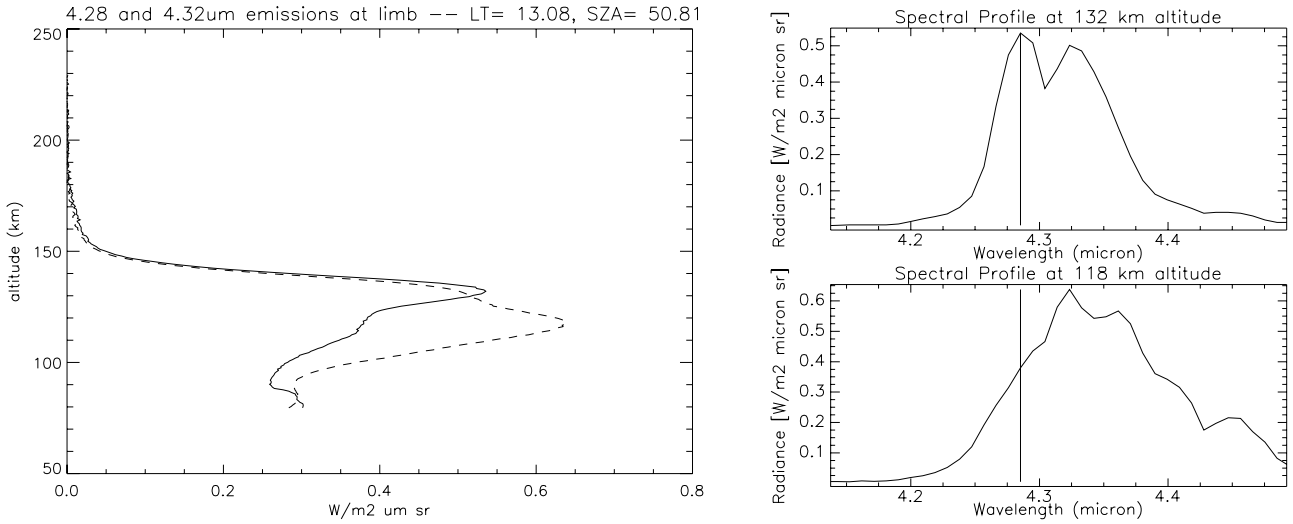

Figure 1. (left) Limb emission profiles at 4.277 μm (solid line) and 4.315 μm (dashed line) on orbit 315. (right) Spectral profiles at 132 km and 118 km altitudes on the limb profile (vertical bar indicates the position of the wavelength at 4.277 μm). The spectral profiles are shifted by about 0.007 μm relative to values indicated in the text owing to a recent correction of spectral registration implemented in the text but not shown.

2007] and their sensitivity to density perturbations, the perturbations of these emissions can be used to characterize the wave content and dynamics of the upper atmosphere and its background circulation.

[5] This study first describes the structure of CO_2 non-LTE emissions at the 4.3 μm wavelength as seen by the VIRTIS-M spectral imaging instrument. The structure and dynamics of wave-like perturbations are then extracted through a specific data processing scheme. Finally, the source of wave excitation and the consequences on Venus circulation models are discussed.

2. CO_2 Non-LTE Emissions at 4.3 μm

[6] The non-LTE CO_2 emissions in the upper atmosphere of Venus are described in detail by *Gilli et al.* [2009] in this issue. These emissions are due to the excitation of CO_2 molecules by dayside solar radiations. Owing to the low atmospheric density above 90 km altitude, these molecules return to their ground state in a noncollisional manner by releasing photons in a series of emission bands around the 4.3 μm wavelength. Non-LTE situations of pure radiative excitation, like the present CO_2 emissions, are relatively insensitive to the actual temperature, while their density dependence is more significant [*Roldán et al.*, 2000; *Lopez-Puertas et al.*, 2000]. In this section, we will recall only the main features of these emissions as seen by VIRTIS-M.

[7] At the spectral resolution of VIRTIS-M, the limb profiles present two main peaks at 4.277 μm and 4.315 μm in the altitude range 110 to 140 km. The first emission peak is weaker than the second and presents a maximum on limb data at higher altitudes. The maximum emission strength and the altitude of the emission centroid vary with solar zenith angle and local time. The centroids of the emissions seen at the limb are in the 125–135 km range at the 4.277 μm wavelength and the 115–120 km range at 4.315 μm. An example of these emissions measured by VIRTIS-M at the limb is shown in Figure 1 for the two emission wavelengths at 1300 local time (LT) and at 50.8° solar zenith angle on orbit 315. In Figure 1, the spectra around the 4.3 μm wavelength clearly show the two emission peaks at 4.277 μm and 4.315 μm plus additional non-LTE emissions above 4.4 μm.

[8] When observed at nadir, CO_2 non-LTE emissions at 4.3 μm show a clear variation with solar zenith angle, as can be seen in Figure 2 from a south polar view acquired during orbits 473 and 474. Some wavelike features, hardly discernible in Figures 2a and 2b, appear over the background emission. The rest of this study will discuss the structure and dynamics of these features. The structure of the background emission is not investigated.

3. Characteristics of Wave Patterns

3.1. Data Processing

[9] This study uses the calibrated VIRTIS-M data for which continuum effects have been removed and absolute spectral radiances are expressed in W/(m^2 μm sr). These data are extracted from the VIRTIS database and processed in the following steps: (1) correction of residual instrument discrepancies between odd and even samples of VIRTIS-M measurement line by an algorithm computing a smooth correction factor for each sample, (2) selection of image parts far from the limb to avoid limb effects, (3) enhancement of wave-like features through a filtering process based on the removal of low-pass filtered background emission, (4) projection of the filtered image into a geographical coordinate system centered on the subspacecraft point to avoid image distortions, (5) computation of wave displacements between two consecutive images for the same wavelength through an algorithm based on cross correlation, and (6) back-projection of the images and estimated displacement and velocity vectors into the true geographical system.

[10] Calibrated VIRTIS-M data are corrected for instrument artifacts such as discrepancies between odd and even

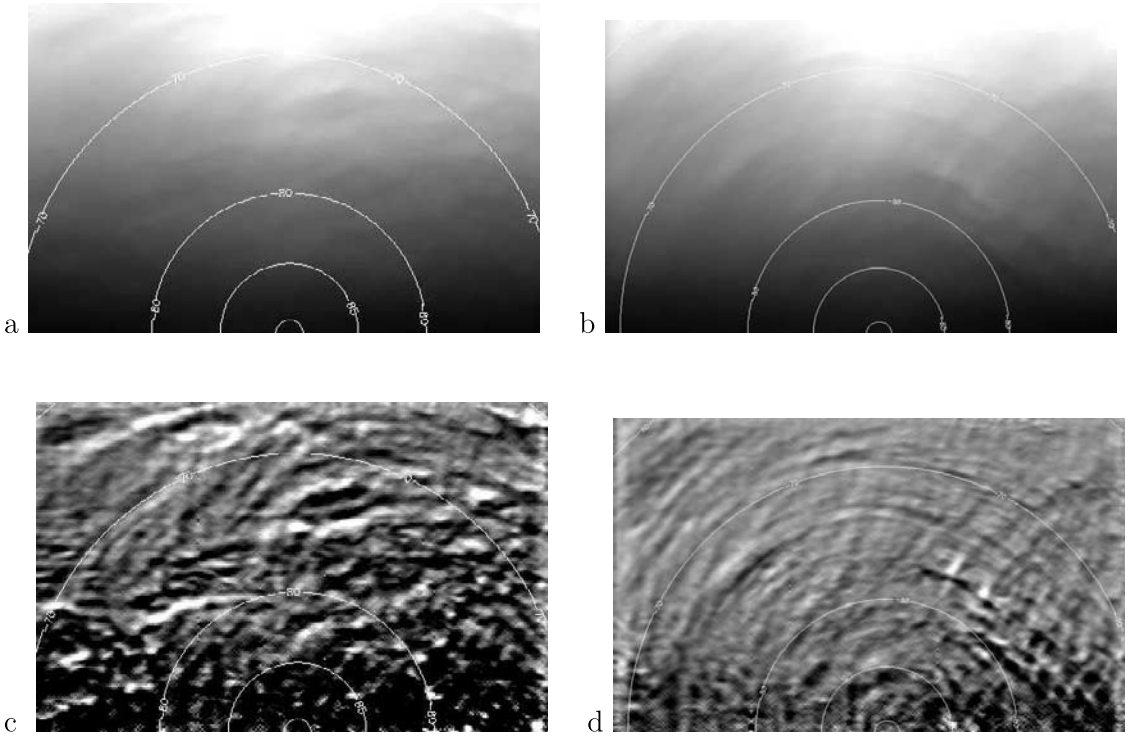

Figure 2. (a and b) Venus south polar views of radiance at the 4.315 μm wavelength averaged over four VIRTIS-M bands, for images taken along orbits 473 (Figure 2a) and 474 (Figure 2b). Color scale from black to white ranges from 0 to 0.06 W/(m$^2\mu$ msr). (c and d) Same images after wave enhancement by the data processing scheme. Color scales range from −1.5 to +1.5% of the background signal on the left (Figure 2c) and from −3 to +3% on the right (Figure 2d). Latitude contours are indicated in degrees, and the terminator line is almost horizontal.

samples along the VIRTIS measurement line. However, owing to the low amplitudes of the wave signals investigated here, an additional correction of this instrument effect is applied in the first step of the algorithm. It is based on the idea that each pixel value at one wavelength p_{ij} is related to the true pixel radiance R_{ij} by a correction factor c_{ij} in the following way: $p_{ij} = R_{ij}c_{ij}$. This correction factor is estimated under the following hypotheses. c_{ij} is smooth along the sample direction (j) because the correction of a given sample is approximately the same for two consecutive measurement lines; and c_{ij} is close to 1 because the relative difference between odd and even samples of VIRTIS-M images is below 10% for more than 95% of the pixels. An algorithm is implemented on the basis of these two assumptions and the true radiance is computed by $R_{ij} = \frac{p_{ij}}{c_{ij}}$.

[11] The second step is carried out manually to exclude regions of the image outside the 50° arc limit around the subspacecraft point. The third step is designed to enhance the wave features on nadir images at the 4.3 μm wavelength. In order to improve the signal-to-noise ratio, the images are first averaged over four VIRTIS-M wavelengths around the first and the second emission peaks (respectively from 4.26 μm to 4.29 μm and from 4.305 μm to 4.335 μm). The background radiation B_{ij} is estimated by low-pass filtering of the radiance values R_{ij} with a median filter 16 pixels wide. The filtered image is then computed through $F_{ij} = R_{ij} - B_{ij}$, and the normalized filtered image is estimated through $N_{ij} = F_{ij}/B_{ij}$. The wave features in these images taken far from the planet, at spacecraft altitudes greater than 20,000 km, have been shown to be almost insensitive to the median filter window for widths larger than 16 pixels. However, even if the use of a median filter is justified to reduce data spike effects, its frequency response is difficult to estimate. The normalized filtered images N_{ij} are used to estimate the amplitudes of the waves relative to the background. Two examples of wave enhancement are presented for CO_2 non-LTE emissions at 4.315 μm in Figures 2c and 2d during orbits 473 and 474. On the nightside, the low level of background signal creates spurious features not shown here. On the dayside, wavefront like features are visible which correspond to the small-scale features observed on the original images.

[12] The projection and back-projection at steps 4 and 6 are performed to avoid distortions of pixels when plotted in geographical coordinates close to the south pole. The average subspacecraft point during the image acquisition is computed, and the pixels coordinates are simply rotated and back-rotated from the true geographical coordinates to a geographical coordinate system in which this point has zero latitude and longitude. In this manner, the latitudes and longitudes of pixels are kept within a range of ±30°. The images are projected on a regular (latitude, longitude) grid of 0.15° resolution in this new coordinate system.

[13] When the VIRTIS data include two images of the same region at different times along the same orbit, the horizontal displacement of the waves can be estimated by cross correlation of the two images. The typical time difference between two consecutive images is about 1800 s. Similarly, if two wavelengths sample different altitudes, the

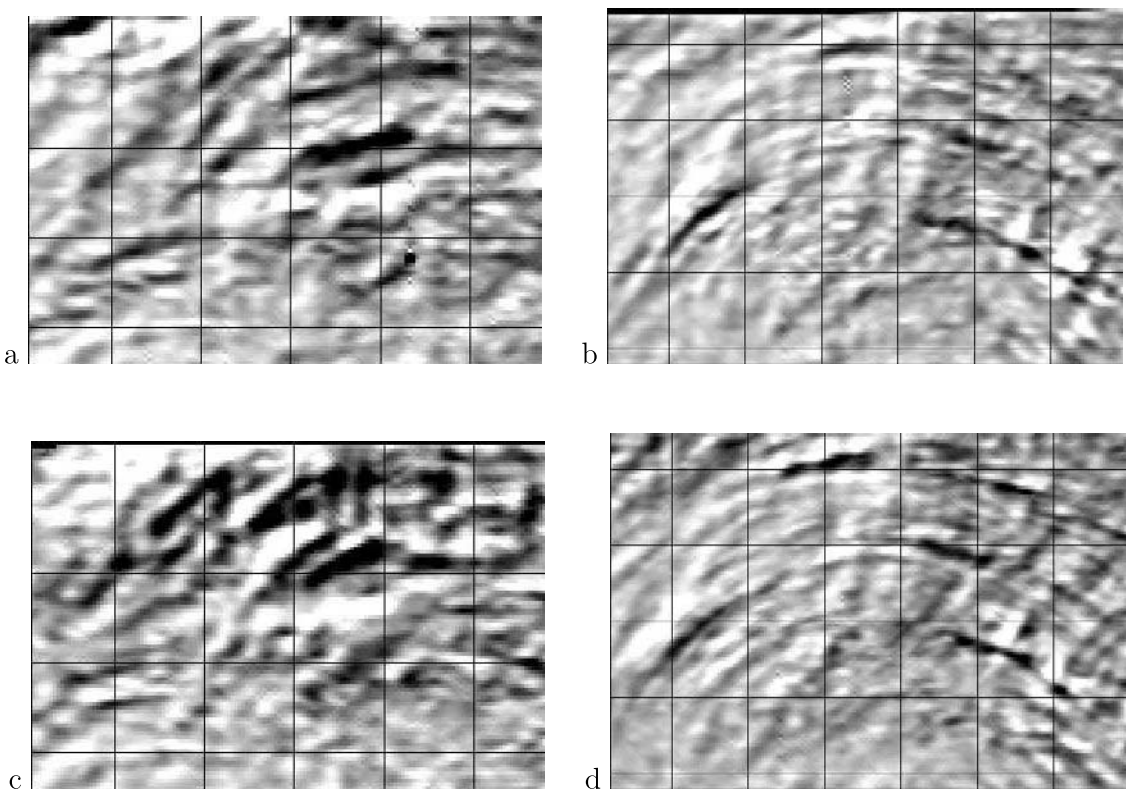

Figure 3. Focus on two consecutive VIRTIS-M images at 4.315 μm wavelength filtered and projected at nadir along orbits (a and c) 473 and (b and d) 474. Color scales range from −1.5 to +1.5% of the background signal on the left and from −3 to +3% on the right. Black grid lines are plotted with a step of 25 pixels equal to the size of the correlation window.

apparent displacement of the wavefront between the two wavelengths on the same image can be used to estimate the vertical wavelength [*Vargas et al.*, 2007]. An important assumption is that the wavefront shape remains constant between the two images. Our method computes the pattern correlation coefficient (PCC) [*Schmetz et al.*, 1993] between two images, defined by

$$PCC_{ij}(n,m) = \frac{\sigma_{12}(n,m)}{\sigma_1 \sigma_2(n,m)} \quad (1)$$

For each point on the first image, located at coordinates (i, j), a square area of K*K pixels centered on this point is defined, and the same square area is defined on the second image centered on the coordinates (i + n, j + m). σ_1 is then the standard deviation of the signal over the area of the first image centered on the (i, j) coordinates, and $\sigma_2(n, m)$ is the standard deviation of the signal over the area of the second image centered on (i + n, j + m) coordinates. $\sigma_{12}(n, m)$ is the covariance of zero mean signals over the two areas. Values of $PCC_{ij}(n, m)$ range from −1 to +1 and are calculated over the range $[-\frac{M}{2}; \frac{M}{2}]$ of indices n and m. The maximum value of this function ($PCC_{ij}^{\max} = PCC_{ij}(n_0, m_0)$) indicates the image shifts (n_0, m_0) at which the two images are best correlated. In order to improve the quality of image shifts retrieved, a minimum value criterion on the correlation is required by $PCC_{ij}^{\max} > 0.8$, and only points with all neighbors fitting this criterion are retained to avoid image border effects. Additionally, the zero shifts values ($n_0 = 0$ and $m_0 = 0$) are excluded because instrument effects generally report a signal at zero shifts. Once the best correlated parts in the images are determined and selected, the image shifts are converted into real displacement between the pixels, and then interpreted as wavefront velocities. This image correlation algorithm has been validated by comparison with outputs of COSI-CORR software [*Leprince et al.*, 2007]. Figure 3 shows examples of consecutive images after filtering and projection at Nadir. In Figure 3, the displacements of wavefronts are clearly visible.

3.2. Wave Structure and Distribution

[14] The VIRTIS-M data containing wave-like features after processing are summarized in Table 1 with corresponding data parameters. These data have been selected from the large VIRTIS-M database because the same region is mapped twice during the same orbit, enabling the computation of the horizontal displacement of wave features at the same wavelength. The VIRTIS-M data covering the 4.3 μm emission on the dayside at nadir are restricted to south pole or terminator views owing to thermal constraints on the instrument.

[15] The two non-LTE emission peaks at the 4.277 μm and 4.315 μm wavelengths show the same patterns after data processing. The image correlation algorithm was not able to detect any coherent horizontal displacement of these patterns between these two wavelengths on the same image. In the rest of the study, only results at the 4.315 μm wavelength are presented because the signal to noise ratio is lower at the 4.277 μm wavelength.

Table 1. Summary of VIRTIS-M Data Providing More Than 100 Horizontal Velocity Estimates and Corresponding Processing Parameters

Orbit	Session	Pixel Size (km)	Range or Dominant Horizontal Wavelength (km)	K/2	M/2	Mean Local Time (h)
219	04	16	340	10	10	11.3
220	01	16	250	10	10	11.5
220	04	16	230	10	10	11.3
232	01	16	210	10	10	11.8
233	01	16	275	10	10	11.8
251	08	16	230	10	10	12.0
473	00–01	16	90–400	12	12	12.3
474	00–01	16	110–320	12	12	13.5
476	00–01	16	90–400	12	12	12.2

[16] The horizontal wavelengths of the upper atmosphere wave features are in the range 90–400 km. The maximum pixel size of VIRTIS-M data in high space resolution mode (about 16.5 km) should make it possible to resolve horizontal wavelengths below 90 km, but such features are rarely seen. Moreover, the various filtering procedures tested do not reveal horizontal wavelengths larger than 400 km. We therefore believe that the horizontal wavelength range of 90–400 km is not biased by instrument resolution or data processing.

[17] Figure 4 shows an example of the typical distribution of wave features observed from south polar view. For comparison between the three images at the 4.315 μm wavelength, the normalized filtered images are plotted with the same scale (±2.5%). On the composite image, coherent circular wavefronts with horizontal wavelengths larger than 200 km are visible in the middle of the image indicating a possible source region close to the south pole. The wave activity is low on the morningside (on the right). On the eveningside (on the left), small horizontal wavelength features (90–200 km) are observed close to dusk with wavefronts almost parallel to the terminator line. The geographical distribution of wave features varies between one orbit and the next, and a wide range of horizontal wavelengths can be observed on the same image, as shown in Figure 2. However, the orientation of wavefronts and the low level of wave activity on the morningside are persistent features.

[18] The root-mean-square (RMS) amplitudes of wave features on all images processed are presented in Figure 5 for the two emission peaks at the 4.277 μm and 4.315 μm wavelengths. The areas over which RMS amplitudes are computed correspond to the image points at which a horizontal velocity vector has been retrieved. The amplitudes of wave-like perturbations of CO_2 non-LTE emissions are slightly larger at the 4.315 μm than at 4.277 μm wavelength. The ratio of RMS wave amplitudes is about 3/4. If the emission radiances are directly interpreted in terms of wave amplitudes, this observation may suggest a wave dissipation between the two emission centroids. However, the unknown sensitivities of non-LTE emissions to density perturbations convolute the wave signal preventing the direct interpretation of emission perturbation amplitudes in terms of wave amplitudes.

3.3. Wave Dynamics

[19] The horizontal displacement of the wave features is computed for the second peak of CO_2 non-LTE emissions (around 4.315 μm) by using the algorithm described in step 5 of data processing. The parameters of the cross-correlation analysis must be adapted to the dominant horizontal wavelength of the signal and to the phase shift between the two images. As shown in Figure 3, the image correlation window size (K) is chosen to be larger than the dominant horizontal wavelength. The displacement range of the correlation window (±M/2) is set to be equal to half the size of the of correlation window (K/2) in order to avoid aliasing. The validity of this parameter was visually checked by comparing image pairs (Figure 3). Parameters K/2 and M/2 chosen for each image pair are given in Table 1, and vary in the range 10–12 pixels. In addition to the quality tests described in the algorithm, the relative difference between horizontal displacement vectors estimated at 4.277 μm and 4.315 μm is computed. Displacement estimates with a relative difference

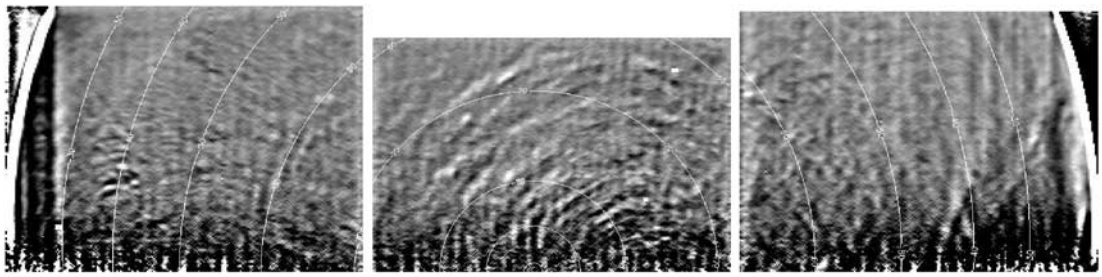

Figure 4. Venus south polar views of normalized filtered images (N_{ij}) at the 4.315 μm wavelength on orbit 232. Black and white color scale ranges from −2.5 to 2.5% on the three images. Latitude contours are indicated in degrees, the terminator line is almost horizontal at the lowest border of the images, and the eveningside (morningside) is on the left (right) side. The data processing generates spurious vertical stripes at the limb owing to the strong contrast there.

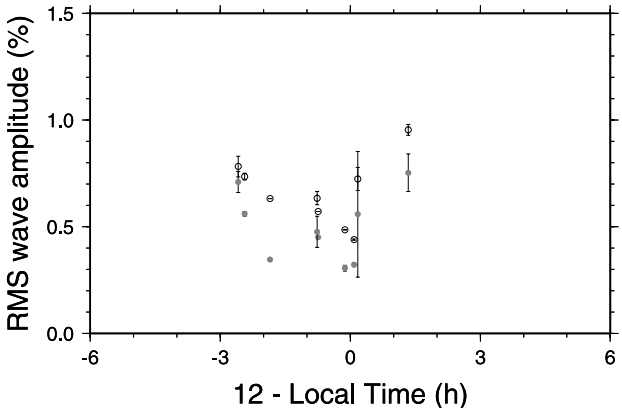

Figure 5. Root-mean-square amplitude (in percent) of wave-like features at the 4.315 μm wavelength (circles) and at 4.277 μm (grey dots) on each image processed as a function of average local time (in hours) in reverse scale (eveningside on the left).

larger than 15% are excluded. From the horizontal displacement estimates and knowing the time lag between the two image points, horizontal phase velocity vectors are calculated.

[20] Some examples of velocity vector estimates are shown in Figure 6 for orbits 473 and 474. The wave velocities are obtained in the part of the image that shows wave features with strong contrasts and which maintain the same shape during the time lag between the two images ($\approx$1800 s). The phase velocity vector is not perpendicular to the wavefront and it presents a strong westward zonal component.

[21] The horizontal velocity vectors for the whole data set are plotted in Figure 7. The amplitudes of the phase velocity vectors are in the 50–110 m/s range. The direction of velocity vectors is zonal westward in the direction of lower atmosphere superrotation, with a small meridional component. The coherency of the velocity vectors is remarkable, because these estimates are obtained from different images along different orbits with different conditions of observation. Meridional and zonal velocities are plotted as a function

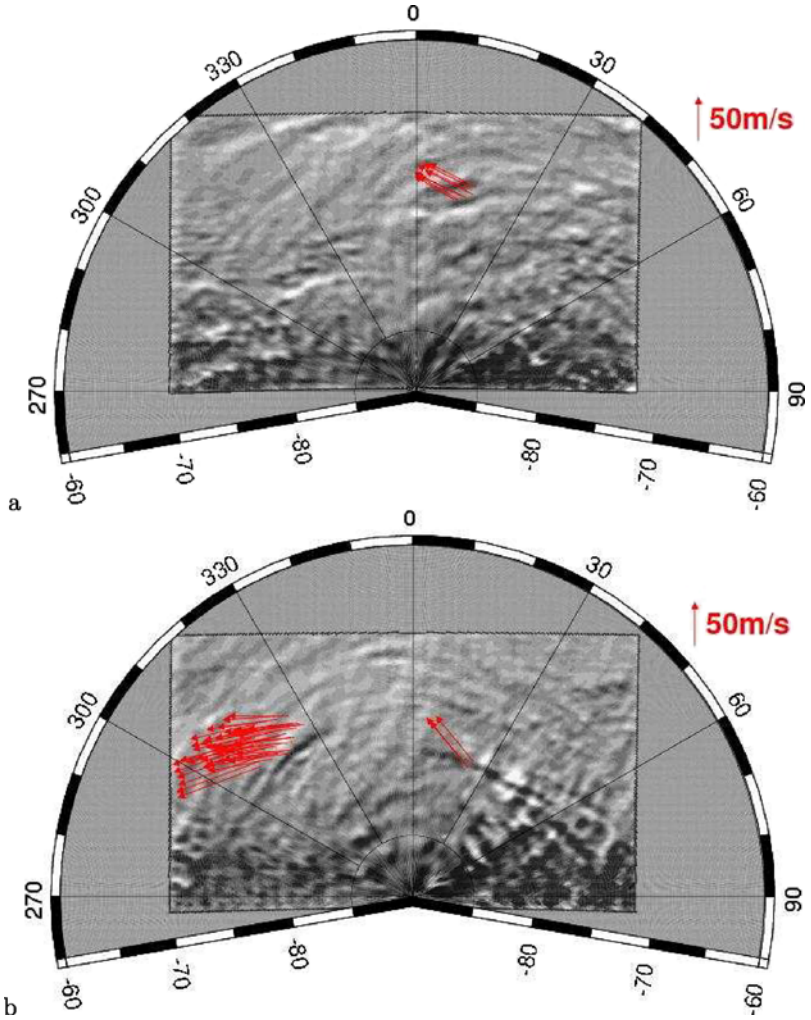

Figure 6. Venus south polar views of enhanced wave features at the 4.315 μm wavelength, and corresponding estimates or horizontal wave velocities along orbits (a) 473 and (b) 474. One velocity estimate in 15 is presented to clarify the plots. Local time is converted into longitude (zero longitude is noon) with evening on the left side.

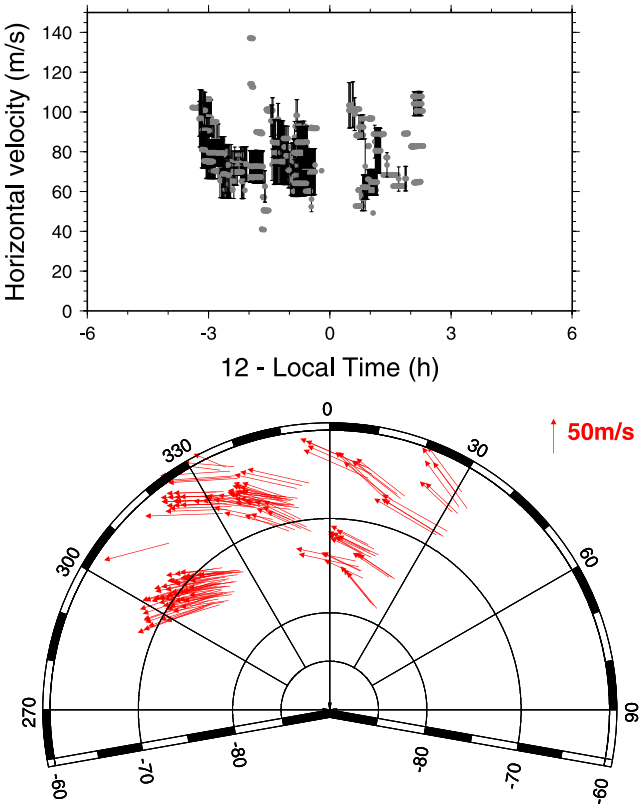

Figure 7. Estimates of horizontal wave velocities. (top) Norm of the horizontal velocity vector (m/s) as a function of local time (h) in reverse scale (eveningside on the left). (bottom) Norm and direction of horizontal velocity vectors as a function of latitude and local time converted into longitude (zero longitude is noon) with evening on the left side. In this plot, one velocity estimate in 15 is presented to clarify the plots.

of local time and latitude on Figure 8. The meridional component is positive (in a northern direction) with an average value of about 30 m/s. The zonal component is westward with an average value of about 70 m/s. The only possible trend in these plots is an increase of the meridional component when approaching dusk, but the low number of images processed in this study did not allow us to validate this feature fully.

3.4. Possible Artifacts and Limitations

[22] The radiance observed at nadir is the sum of the direct non-LTE emission and possible other components coming from the reflection of these emissions and/or the sunlight on cloud top at these wavelengths. In order to check the possible contribution of light reflected on cloud top, the wave enhancement procedure was applied on the same images at the 2.9 μm wavelength and in the visible for which the reflected sunlight is the main contribution. Some wave features were detected on these images, but the positions and orientations of these features are completely different from the ones observed at the 4.3 μm wavelength. Similarly, the background emission observed at the 4.3 μm wavelength and its large horizontal wavelength variations are different from the ones observed in the visible and at the 2.9 μm wavelength. So, the reflected light on cloud top is not the main contribution at the 4.3 μm wavelength.

[23] Our data processing scheme is limited to integer pixel displacements, but this limitation will be overcome in future subpixel versions by interpolation of the correlation function or by analysis in the frequency domain [*Leprince et al.*, 2007]. The main limitation comes from the low signal to noise of the wave features partly owing to their low amplitude relative to background emission and partly owing to operational constraints on the spacecraft orientation and on VIRTIS-M exposure time. However, the strong consistency of our results, obtained along different orbits for different observation conditions, excludes the possibility of these wave features having been created by noise or artifacts.

[24] Another limitation of our analysis arises from the integrated character of the 4.3 μm radiance along the line of sight. In order to fully interpret these data it is necessary to know the large wavelength space/time variations of non-LTE CO_2 volumetric emission, and the sensitivity of these emissions to density perturbations. The first parameter will be obtained from an analysis of the whole VIRTIS data set, including limb profiles, and the second will be modeled as an extension of previous modeling [*Roldán et al.*, 2000; *Lopez-Puertas and Lopez-Valverde*, 1995; *López-Valverde et al.*, 2007].

4. Interpretation

4.1. Wave Type

[25] In order to identify the type and structure of the observed wave features, the results are analyzed in the framework of gravity and acoustic wave propagation theories. The difficulty when discussing the wave type (gravity or acoustic waves) lies in the following two major unknowns: the vertical wave structure and the background circulation. The vertical wave structure can be constrained by the thickness of the emission layers and the fact that the two main non-LTE emissions at 4.277 μm and 4.315 μm display the same wave features whereas their centroid altitudes seen at the limb are separated by about 15 km. These two observations impose a minimum vertical wavelength of approximately 30 km. Concerning the background thermospheric circulation, previous models [*Zhang et al.*, 1996; *Bougher et al.*, 1997] predict a strong subsolar to antisolar circulation with winds in the range 60–130 m/s in this altitude range (110–140 km) and in this angular distance range to the terminator (15°–35°). However, the particularities of the atmospheric dynamics in the polar region [*Piccioni et al.*, 2007] can modify this simple picture significantly.

[26] The wavefronts are almost parallel to lines of constant latitude, so the horizontal component of the apparent phase velocity (C_0^h) can be approximated by the meridional component of the phase velocity which is perpendicular to the wavefronts. An average apparent horizontal phase velocity is $C_0^h = 30 \pm 10$ m/s. If we assume that our wave features are acoustic waves, the intrinsic horizontal phase velocity is $C_i^h = C_0^h - U$, with the background meridional wind U in the range [−130;0] m/s, which is a very conservative hypothesis. We deduce that C_i^h is in the range [20;170] m/s taking into account error bars. The speed of sound at these altitudes is about 215 m/s. Because this value is a minimum estimate of the intrinsic horizontal phase

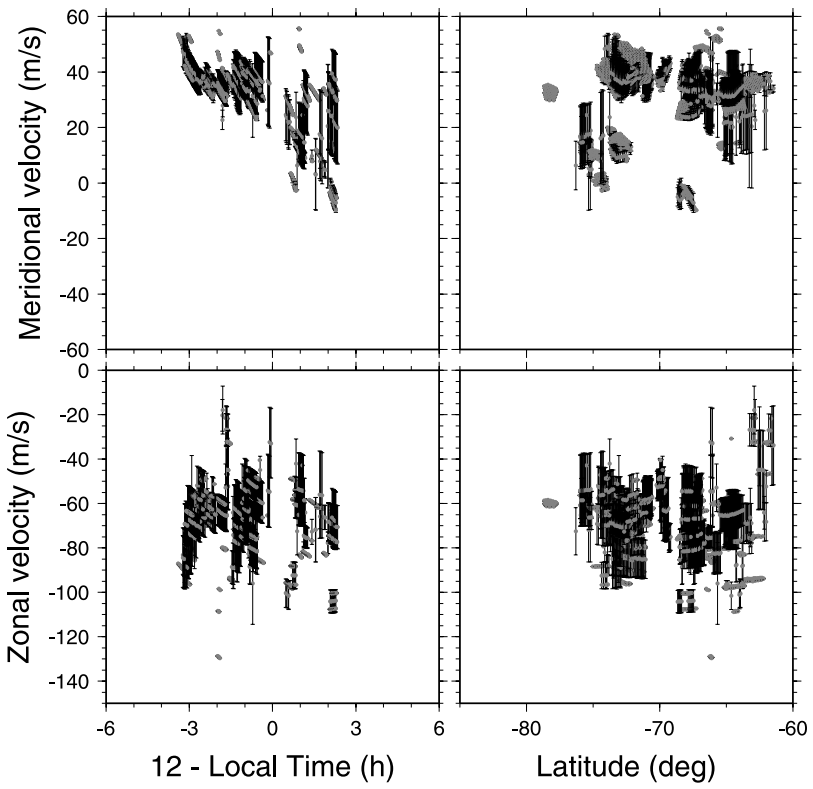

Figure 8. (top) Meridional and (bottom) zonal components of the apparent phase velocities as a function of (left) local time in reverse scale and (right) latitude.

velocity C_i^h for acoustic waves, obtained only for horizontal wave propagation, our wave features cannot be acoustic waves. So, the gravity wave hypothesis is the only remaining possibility.

[27] In conclusion, the wave features presented here are indicative of gravity wave phenomena. We will explore in the next two sections the source and propagation of these waves and their links to the background atmospheric dynamics.

4.2. Gravity Wave Source

[28] As shown in Figures 4 and 6 the main wavefronts are almost circular and parallel to lines of constant latitude. This observation suggests a source close to the south pole. Figure 9 shows a comparison between the enhanced wave features at the 4.315 μm wavelength and the polar vortex observed at the 5.05 μm wavelength in the same images. This comparison has also been performed on polar vortex features observed at the 3.3 μm wavelength (which is less sensitive to saturation problems) for all the images processed in this study. The direction perpendicular to wavefronts is always pointing in the direction of the region of strongest polar vortex activity, whatever the position and shape of the vortex. These observations clearly identify the polar vortex as the source of the gravity waves observed in the 110–140 km altitude range. This conclusion is also supported by theoretical studies [*Baker et al.*, 1999; *Nappo*, 2002] which demonstrate that turbulence is able to generate gravity waves propagating upward. For such a source close to south pole, the gravity waves propagate with horizontal components of intrinsic phase and group velocities along meridional direction from the pole to the equator.

[29] Moreover, the analysis of VIRTIS-M images has shown that the wave features at the 4.315 μm wavelength are more numerous with larger amplitude when the polar vortex is on the dayside than on the nightside. As an example, Figures 10a and 10b show that only a few wave features of low amplitude are visible when the polar vortex is completely on the nightside. This observation suggests that the gravity wave propagation from the cloud layer up to the 110–140 km altitude range is more favorable on the dayside than on the nightside. Figure 10c shows the Brunt-Väisälä frequency profile computed for day and night Venus atmosphere parameters [*Hunten et al.*, 1983]. In the 100–140 km range, it increases on the nightside and decreases on the dayside. The shape of the Brunt-Väisälä frequency profile on the dayside suggests that gravity waves may be trapped between altitudes of 60 km to 140 km for wave frequencies between 3 and 3.5 mHz. In this layer, trapped waves propagate horizontally with horizontal wavelengths depending on the trapped mode number, and with low attenuation along their path [*Lighthill*, 2001]. The presence of these trapped waves at frequencies higher than 3 mHz could explain the difference between day and nightside observations. Moreover, the presence of strong background winds and vertical wind variations may also play an important role in the day/night difference of wave propagation by creating wind ducts [*Nappo*, 2002; *Snively et al.*, 2007; *Zhou and Morton*, 2007].

4.3. Implications for Background Circulation

[30] The gravity waves at these heights propagate within the global thermosphere circulation. The horizontal phase

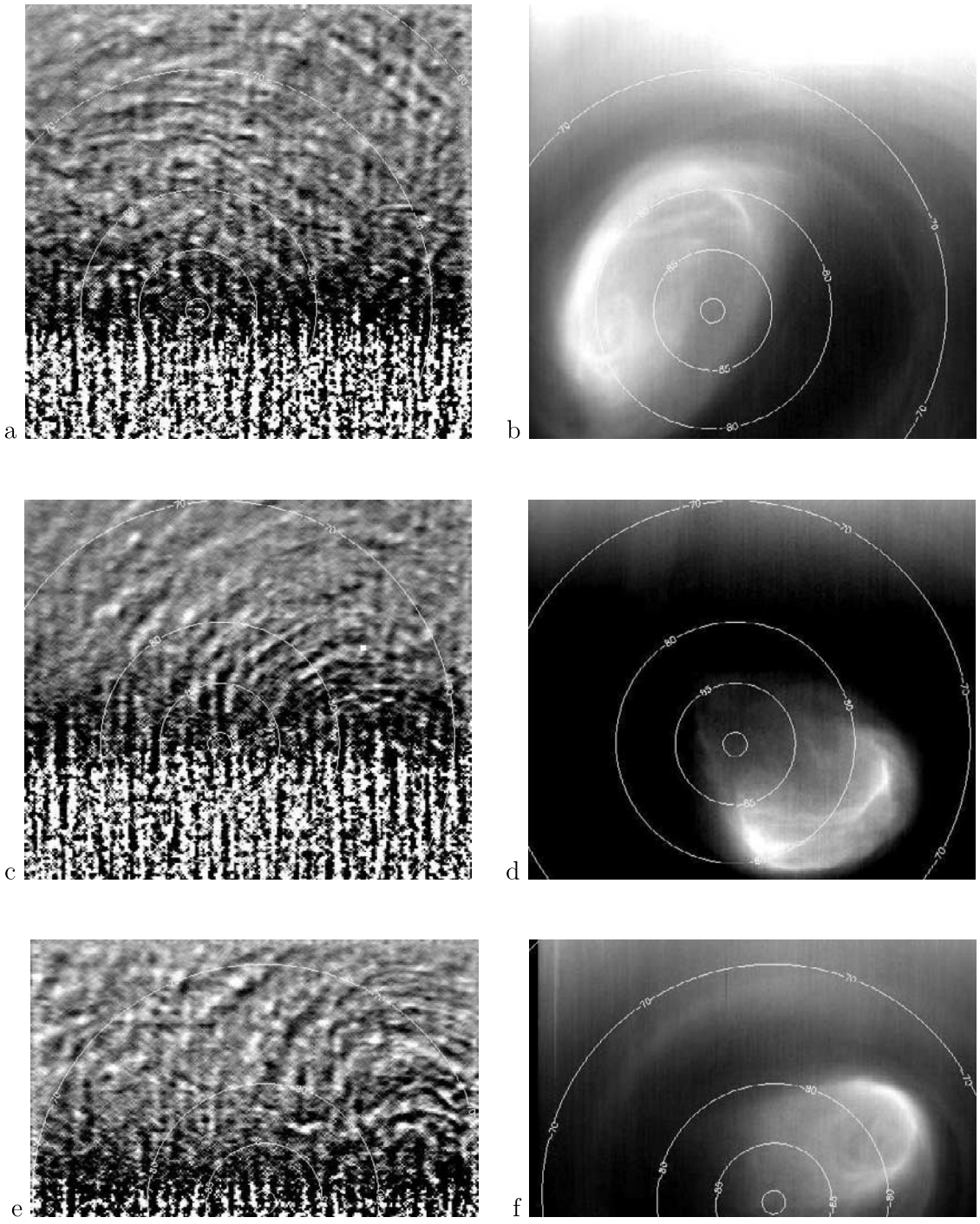

Figure 9. Venus south polar views along orbits (a and b) 220, (c and d) 232, and (e and f) 251 of (left) enhanced wave features at 4.315 μm wavelength and (right) emission at 5.05 μm wavelength which reveals the structure and position of the south polar vortex. Latitude contours are indicated in degrees, and the terminator line is clearly visible through the spurious features created by the data filtering on the nightside.

speeds obtained therefore include the effects of both wave propagation and background wind. Consequently, the observed gravity wave propagation can constrain the background wind structure.

[31] If we assume that the source of the gravity waves is the turbulent area of the polar vortex close to the south pole, their propagation without wind should be mainly along meridians. However, a strong zonal component of the horizontal phase velocity is observed in Figures 7 and 8. This observation implies that a zonal westward background wind of about 70 m/s is present at the altitude of 4.315 μm wavelength non-LTE emission perturbations in the 0900–1500 LT range in the polar regions. The gravity wave propagation therefore suggests that the zonal lower

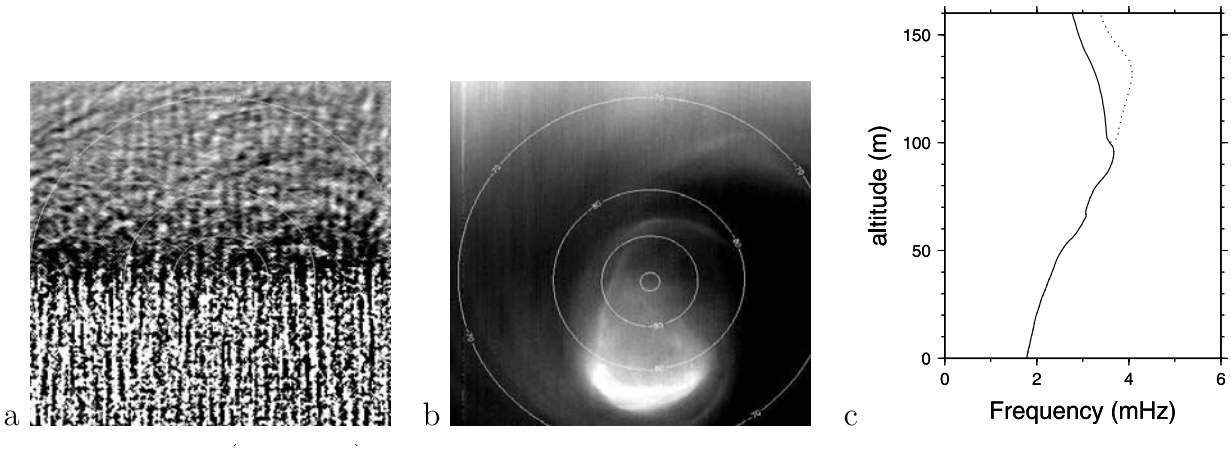

Figure 10. Venus south polar views along orbit 253 of (a) enhanced wave features at the 4.315 μm wavelength and (b) emission at the 5.05 μm wavelength revealing the structure and position of the south polar vortex. Latitude contours are indicated in degrees. (c) Plot of the Brunt-Väisälä frequency (in mHz) as a function of altitude (in km) on the dayside (solid line) and on the nightside (dotted line), computed for Venus atmosphere models [*Hunten et al.*, 1983].

thermosphere circulation in the 0900–1500 LT range is in the direction of the lower atmosphere superrotation up to 30° from the south pole and up to an altitude of at least 115 km.

[32] Moreover, because of the absence of phase difference between the wave features observed at the 4.277 μm and 4.315 μm wavelengths, the vertical wavelength of these waves must be larger than twice the centroid altitude difference of these two emissions (≈15 km at the limb) [*Vargas et al.*, 2007]. In order to use this constraint, the gravity wave dispersion relation with constant background wind should be written [*Li et al.*, 2007]

$$\frac{N^2}{(C_0 - U)^2} = m^2 + k^2 + \frac{1}{4H^2} \tag{2}$$

where $m = \frac{2\pi}{\lambda_z}$ is the vertical wave number with λ_z the vertical wavelength, $N = 2\pi f = 0.0215$ rad/s (or $f = 3.4$ mHz) is the Brunt-Väisälä pulsation which is estimated from a dayside Venus atmosphere model at a latitude of 120 km [*Hunten et al.*, 1983], C_0 is the apparent wave velocity, U is the meridional wind, $k = 2.513 \times 10^{-5}$ rad/m is the horizontal wave number assuming an average 250 km horizontal wavelength, and $H = 4$ km is the density scale height at 120 km altitude. If we assume an intrinsic wave propagation from the pole to the equator, and a lower bound on the vertical wavelength $\lambda_z > 2 * 15$ km = 30 km and on the apparent phase velocity $C_0 > C_0^h = 30$ m/s, by using equation (2) we deduce an upper bound on the meridional phase velocity $U < -58$ m/s. This analysis suggests that the meridional wind is opposite to the wave propagation direction with an amplitude greater than about 60 m/s. This conclusion is in favor of a subsolar to antisolar thermospheric meridional circulation consistent in direction and amplitude with previous results [*Zhang et al.*, 1996; *Bougher et al.*, 1997].

[33] In addition to the gravity wave dispersion analysis, the previous conclusion is also supported by the geographical distribution of gravity wavefronts. *Sun et al.* [2007] demonstrated recently that gravity waves propagating against the wind direction are amplified relative to other propagation directions. Assuming a wave source close to the south pole and a strong subsolar to antisolar wind, this prediction is consistent with our observation of gravity wave features above the noise level only in the 0900–1500 LT range. The wave feature distribution therefore also supports the presence of a strong subsolar to antisolar wind at the south pole.

5. Conclusion

[34] The nadir images of non-LTE CO_2 emissions present wave-like perturbations of about 0.5% RMS amplitude relative to background signal. These features are mainly observed in the 0900–1500 LT range, and their horizontal wavelengths are in the 90–400 km range. The dynamics of these wave features are similar for all the images processed along different orbits. Average zonal and meridional components of the horizontal phase velocities are respectively 70 m/s westward and 30 m/s northward. The horizontal phase velocities and horizontal wavelengths are compatible with gravity waves propagating in the 110–140 km altitude range which is sampled by non-LTE CO_2 emissions at the 4.3 μm wavelength. The considerable uncertainty on the altitude of these perturbations restricts the acquisition of information on the vertical structure of the waves. However, the geographical distribution and the orientation of wavefronts clearly identify the polar vortex at work in the cloud layer as the source of gravity waves. Finally, the characteristics of gravity wave propagation can be used to infer the background atmospheric winds. The strong zonal component of gravity wave phase velocities is not due to their propagation from a source close to the south pole, and can consequently be attributed to the background atmospheric circulation in the 110–140 km altitude range. The gravity wave dispersion relation and the geographical distribution of wavefronts strongly argue in favor of the presence of a subsolar to antisolar wind of amplitude larger than 60 m/s close to the south pole.

[35] This first direct mapping of thermospheric gravity waves demonstrates the strong influence of the polar vortex on the atmospheric polar circulation of Venus [*Piccioni et al.*, 2007], and illustrates an upward energy transfer from the cloud layer to the thermosphere. Moreover, this study seems to demonstrate the persistence of superrotation dynamics at least up to 115 km in polar regions (up to 30° from the south pole). Furthermore, our data support the existence of the subsolar to antisolar circulation predicted by thermosphere circulation models [*Zhang et al.*, 1996; *Bougher et al.*, 1997], with meridional wind speeds greater than 60 m/s in this polar region.

[36] The increase of the VIRTIS database will improve the statistics of wave features, and its combination with VMC data [*Markiewicz et al.*, 2007] will make it possible to follow gravity wave propagation from the top of the cloud layer up to the thermosphere. In order to improve our description and understanding of these wave phenomena, a large-scale three-dimensional model of CO_2 volumetric emission rates should be developed by using the limb and nadir VIRTIS observations, the sensitivity of these emissions to gravity wave perturbations should be modeled, and the gravity wave propagation within the background circulation should be computed. Finally, these high-altitude emissions can also be used to investigate transient infrasonic signals generated by quakes and volcanic events [*Garcia et al.*, 2005].

[37] **Acknowledgments.** Two anonymous reviewers improved this paper considerably by their constructive comments. We thank Stéphane Erard and Alejandro Cardesin for computation and validation of VIRTIS-M data and corresponding observation geometry, Ricardo Hueso Alonso for his help with IDL data projection routines, F. Ayoub for his help with COSI-CORR software, Sébastien Lebonnois for helpful discussions on the atmosphere dynamics, and P.E. Mallet for validating the correlation software. This study was funded by CNES through space research scientific projects.

References

Alexander, M. (1992), A mechanism for the Venus thermospheric superrotation, *Geophys. Res. Lett.*, *19*, 2207–2210.

Baker, R., G. Schubert, and P. Jones (1999), High rayleigh number compressible convection in Venus' atmosphere: Penetration, entrainment, and turbulence, *J. Geophys. Res.*, *104*, 3815–3832.

Bougher, S., and W. Borucki (1994), Venus O_2 visible and IR nightglow: Implications for lower thermosphere dynamics and chemistry, *J. Geophys. Res.*, *99*, 3759–3776.

Bougher, S., M. Alexander, and H. Mayr (1997), Upper atmosphere dynamics: Global circulation and gravity waves, in *Venus II: Geology, Geophysics, Atmosphere, and Solar Wind Environment*, edited by S. W. Bougher et al., pp. 259–291, Univ. of Ariz. Press, Tucson.

Drossart, P., et al. (2004), VIRTIS imaging spectrometer for the ESA/Venus Express mission, in *Earth Observing Systems IX*, vol. 5583, pp. 175–185, Int. Soc. for Opt. Eng., Bellingham, Wash.

Drossart, P., et al. (2007), A dynamic upper atmosphere of Venus as revealed by VIRTIS on Venus Express, *Nature*, *450*, 641–645, doi:10.1038/nature06140.

Garcia, R., P. Lognonné, and X. Bonnin (2005), Detecting atmospheric perturbations produced by Venus quakes, *Geophys. Res. Lett.*, *32*, L16205, doi:10.1029/2005GL023558.

Gierasch, P. (1987), Waves in the atmosphere of Venus, *Nature*, *328*, 510–512.

Gierasch, P., et al. (1997), The general circulation of the Venus atmosphere: An assessment, in *Venus II: Geology, Geophysics, Atmosphere, and Solar Wind Environment*, edited by S. W. Bougher et al., pp. 459–500, Univ. of Ariz. Press, Tucson.

Gilli, G., M. López-Valverde, P. Drossart, G. Piccioni, S. Erard, and A. Cardesín-Moinelo (2009), Limb observations of CO_2 and CO non-LTE emissions in the Venus atmosphere by VIRTIS/Venus Express, *J. Geophys. Res.*, doi:10.1029/2008JE003112, in press.

Hinson, D., and J. Jenkins (1995), Magellan radio occultations measurements of atmospheric waves on Venus, *Icarus*, *114*, 310–327.

Hunten, D., L. Colin, T. Donahue, and V. Moroz (Eds.) (1983), *Venus*, 1143 pp., Univ. of Ariz. Press, Tucson.

Kasprzak, W. T., H. B. Niemann, A. E. Hedin, and S. W. Bougher (1993), Wave-like perturbations observed at low altitudes by the Pioneer Venus Orbiter Neutral Mass Spectrometer during orbiter entry, *Geophys. Res. Lett.*, *20*, 2755–2758.

Leprince, S., S. Barbot, F. Ayoub, and J. Avouac (2007), Automatic and precise ortho-rectification, coregistration, and subpixel correlation of satellite images: Application to ground deformation measurements, *IEEE Trans. Geosci. Remote Sens.*, *45*, 1529–1558.

Li, F., G. Swenson, A. Liu, M. Taylor, and Y. Zhao (2007), Investigation of a wall wave event, *J. Geophys. Res.*, *112*, D04104, doi:10.1029/2006JD007213.

Lighthill, J. (2001), *Waves in Fluids*, 520 pp., Cambridge Univ. Press, Cambridge, U.K.

Lopez-Puertas, M., and M. A. Lopez-Valverde (1995), Radiative energy balance of CO2 non-LTE infrared emissions in the Martian atmosphere, *Icarus*, *114*, 113–129, doi:10.1006/icar.1995.1047.

Lopez-Puertas, M., M. Lopez-Valverde, R. Garcia, and R. G. Roble (2000), A review of CO2 and CO abundances in the middle atmosphere, in *Atmospheric Science Across the Stratopause*, *Geophys. Monogr. Ser.*, vol. 123, edited by D. E. Siskind, S. D. Eckermann, and M. E. Summers, pp. 83–100, AGU, Washington D.C.

López-Valverde, M.A., P. Drossart, R. Carlson, R. Mehlman, and M. Roos-Serote (2007), Non-LTE infrared observations at Venus: From NIMS/Galileo to VIRTIS/Venus Express, *Planet. Space Sci.*, *55*, 1757–1771, doi:10.1016/j.pss.2007.01.008.

Markiewicz, W., et al. (2007), Morphology and dynamics of the upper cloud layer of Venus, *Nature*, *450*, 633–636, doi:10.1038/nature06320.

Mayr, H. G., I. Harris, W. T. Kasprzak, M. Dube, and F. Varosi (1988), Gravity waves in the upper atmosphere of Venus, *J. Geophys. Res.*, *93*, 11,247–11,262.

Nappo, C. (2002), *An Introduction to Atmospheric Gravity Waves*, 276 pp., Academic, San Diego.

Piccioni, G., et al. (2007), South-polar features on Venus similar to those near the north pole, *Nature*, *450*, 637–640, doi:10.1038/nature06209.

Roldán, C., M. López-Valverde, and M. López-Puertas (2000), Non-LTE infrared emissions of CO2 in the atmosphere of Venus, *Icarus*, *147*, 11–25.

Schmetz, J., K. Holmlund, J. Hoffman, B. Strauss, B. Mason, V. Gaertner, A. Koch, and L. Van De Berg (1993), Operational cloud-motion winds from Metosat infrared images, *J. Appl. Meteorol.*, *32*, 1206–1225.

Snively, J. B., V. P. Pasko, M. J. Taylor, and W. K. Hocking (2007), Doppler ducting of short-period gravity waves by midlatitude tidal wind structure, *J. Geophys. Res.*, *112*, A03304, doi:10.1029/2006JA011895.

Sun, L., W. Wan, F. Ding, and T. Mao (2007), Gravity wave propagation in the realistic atmosphere based on a three-dimensional transfer function model, *Ann. Geophys.*, *25*, 1979–1986.

Vargas, F., G. Swenson, A. Liu, and D. Gobbi (2007), O(1S), OH, and O2(b) airglow layer perturbations due to AGWs and their implied effects on the atmosphere, *J. Geophys. Res.*, *112*, D14102, doi:10.1029/2006JD007642.

Woo, R., J. W. Armstrong, and A. Ishimaru (1980), Radio occultation measurements of turbulence in the Venus atmosphere by Pioneer Venus, *J. Geophys. Res.*, *85*, 8031–8038.

Woo, R., J. W. Armstrong, and A. J. Kliore (1982), Small-scale turbulence in the atmosphere of Venus, *Icarus*, *52*, 335–345, doi:10.1016/0019-1035(82)90116-6.

Young, R. E., R. L. Walterscheid, G. Schubert, A. Seiff, V. M. Linkin, and A. N. Lipatov (1987), Characteristics of gravity waves generated by surface topography on Venus: Comparison with the VEGA balloon results, *J. Atmos. Sci.*, *44*, 2628–2639.

Zhang, S., S. Bougher, and M. Alexander (1996), The impact of gravity waves on the Venus thermosphere and O_2 IR nightglow, *J. Geophys. Res.*, *101*, 23,195–23,205.

Zhou, Q., and Y. Morton (2007), Gravity wave propagation in a nonisothermal atmosphere with height varying background wind, *Geophys. Res. Lett.*, *34*, L23803, doi:10.1029/2007GL031061.

P. Drossart, LESIA, Observatoire de Paris, UPMC, Université Paris-Diderot, CNRS, 5 place Jules Janssen, F-92195 Meudon, France.

R. F. Garcia, Laboratoire de Dynamique Terrestre et Planétaire, UMR5562, Observatoire Midi-Pyrénées, Université de Toulouse, 14 avenue Edouard Belin, F-31400 Toulouse, France. (garcia@dtp.obs-mip.fr)

M. López-Valverde, Instituto de Astrofísica de Andalucía, CISC, 50 Camino Bajo de Huétor, ES-18080 Granada, Spain.

G. Occhipinti, Institut de Physique du Globe de Paris, Université Denis Diderot Paris 7, 4 place Jussieu, F-75252 Paris CEDEX 05, France.

G. Piccioni, INAF, IASF, via del fosso del cavaliere 100, I-00133 Rome, Italy.